September 2024, Vol:2, Issue:2

International Journal of New Findings in Engineering, Science and Technology

journal homepage: *https://ijonfest.gedik.edu.tr/*

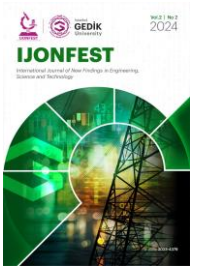

Monte Carlo simulation of distance-dependent quantum entanglement in mixed XXZ Heisenberg spin-1/2 chains

İzzet Paruğ DURU[a*], Şahin AKTAŞ[b]

[a]*Istanbul Gedik University, Medical Imaging Technics Program, Istanbul, Türkiye e-mail:parug.duru@gedik.edu.tr(*Corresponding Author)*
[b] *Marmara University, Faculty of Science, Department of Physics, Istanbul, Türkiye e-mail:saktas@marmara.edu.tr*

Abstract

The quantum entanglement of mixed XXZ Heisenberg spin-1/2 chain is examined. We quantify localizable entanglement (LE) in terms of upper/lower bounds through Quantum Monte Carlo simulations. Loop algorithm is chosen to numerically calculate thermodynamic quantities including spin-spin correlations. The exchange coupling, Zeeman energy, and dipolar interaction are taken into account. Findings summarize that the strength of dipole-dipole interaction (D) and external magnetic field (Bz) are notable in entanglement formation driving the creation and extinction of entanglement. The creation and extinction of entanglement depend on D and Bz. Furthermore, strong fields at critical temperatures lead to a non-monotonic/monotonic behavior introducing revival phenomena. Nevertheless, strong D provides the distance-dependent stability of LE values, preserving unity.

Keywords: Mixed magnetic state; Quantum entanglement; Monte Carlo simulation; Revival phenomena; Critical temperature.

1. INTRODUCTION

A significant information resource is provided by entanglement, which is a notable aspect of executing quantum information operations like quantum teleportation [1-3] and quantum computation [4-9]. Since their literal and straightforward construction makes them ideal for studying entanglement and strong correlations, Heisenberg and Ising-like models, determining the magnetic state of a spin system [10, 11], have been notably preferred. Additionally, a remarkable number of studies revealing magnetic characterization and particularly spin-spin correlations have been performed [12-19]. Since 1D-spin arrays, which considerably incorporate entangled states, can be presented as a credible choice for quantum information operations, have exhaustively concentrated on the Heisenberg Hamiltonian introducing quantum spin-1/2 chains [20-23]. Additionally, they concentrated on the concurrence of mixed states of two qubits. Wang concludes that zero-field concurrence has unity at low temperatures until T = 0.2, and vanishes at T = 1.1 [24]. For an isotropic XY chain, however, a quantum phase transition for a critical value of B is observed at zero temperature [25].

https://doi.org/10.61150/ijonfest.2024020206

Copyright © 2024 IJONFEST

For the isotropic XXX model (J = 1), entanglement disappeared at T = 0.9, according to Rigolin's calculations [26]. In addition to measuring the concurrence of the two nearby spins, multi-particle entanglement can yield useful information between distant pairs of spins. An eligible measurement tool is LE. Androvitsaneas et al. seek a close relation between LE and anisotropy in the case of XY and XYZ models in the absence/presence of the applied magnetic field reporting Bz = 0.75 as a quantum critical point. Besides, rival regions under specific magnetic fields and thermal agitations are displayed for the 10 closest neighboring spins [27]. Spherical nanostructures are dressed with dipoles by Sinyagin et al. to ascertain the aggregation of the considered structure [28]. A strong argument for ~~a~~ topological storage may be ensured through inevitably long-distant entangled couples [29]. However, [30] examined the two-qubit long-range entanglement and revealed the coupling of qubits across long distances. There is also a wealth of possible research material for several long-ranged interacted systems [31-41]. Several experimental investigations utilizing low-dimensional quantum-spin models have been conducted to explore the characteristics of quasi-particle excitations [39, 40, 42]. Sahling evaluates the first example of entangled spins in bulk materials at relatively low temperatures [43].

In theory, it is necessary to comprehend quantum phase transitions in the context of condensed matter physics [44-46]. The dipole-dipole interaction under transverse magnetic field stressing a quantum phase transition on antiferromagnetic (AFM) spin chains is underlined by Bravo et al. [46]. We have previously concentrated on quantifying LE of an AFM spin-chain taking the dipolar interaction (D) and the external magnetic field (Bz) into account. Rival zones are connected to the temperature for specific values of D and Bz [47]. Under a uniform external magnetic field (Bz), this work highlights the impact of dipole-dipole interaction (D) on the upper and lower bounds of entanglement in isotropic ferromagnetic spin-1/2 Heisenberg chains. The ALPS package [48] is preferred to calculate and simulate the model by loop algorithm to specify LE in terms of upper and lower bounds. LE is a useful tool to figure out how much a multipartite system is entangled, measuring bipartite entanglement. It quantifies the average maximal entanglement between two parts of the system by performing local measurements throughout the rest of the system [49-51]. LE and the entanglement of assistance are connected (EoA). The authors have built a Phyton script for post-processing simulation data. Our objective is to address the impact of dipolar interaction on LE using numerical methods. Additionally, we sought to measure the entanglement of long-ranged neighboring spins in multipartite systems.

In this article, the Hamiltonian and expectation values using a loop algorithm and Quantum Monte Carlo techniques are described in Section 2. In Section 3, the determination of upper and lower bounds of localizable entanglement is discussed. Temperature, spin-spin interaction, strength of dipolar interaction, and additionally external magnetic field are taken into consideration related to the n neighboring spins. Section 4 includes a summary of the findings.

2. MODEL & METHOD

2.1 Background of Loop Algorithm

The Loop algorithm [57-59], has been first developed in “Lattice 91” (Tsukuba, Japan) as a Quantum Monte Carlo procedure. It overcomes almost all the difficulties of world-line algorithms by considering non-local changes in the world-line configuration determined by local stochastic decisions. Moreover, it can be comprehensively applied to numerous models, including stochastic series expansion (SSE) [60-62], and the imaginary time world lines formulation [63]. It corresponds to the cluster algorithms developed by Swendsen-Wang [64] in a classical statistical system. Main features: autocorrelations are reduced, it can be easily formulated for continuous time Monte Carlo (by eliminating the Trotter approach), and observables can be formulated in terms of loop features by reducing the errors of the quantities measured with Improved Estimators. Besides, non-diagonal operators can be measured with advanced evaluators and the sign problem can be overcome (especially in fermionic systems). However, it can be coded more easily than traditional worldlines.

Copyright © 2024 IJONFEST

S_p, given in Equation 1, corresponds to the possible spin local configurations where eigenvalues are $S_{i,j}^z = \mp 1/2$ constrained through z direction.

$$S_p \equiv (S_{i,j}^z, S_{i+1,j}^z, S_{i,j+1}^z, S_{i+1,j+1}^z) \quad (1)$$

The statistical weight of the entire possible configurations can be represented by $W(s_P)$ in a density matrix formalism. Equation 2 contains probable spin configurations including the Heisenberg Hamiltonian, $\hat{H}_i$, which operates spin-1/2 pairs exponentially.

$$W(s_P) \equiv \langle S_{i,j}^z, S_{i+1,j}^z | e^{-\Delta\tau \hat{H}_i} | S_{i,j+1}^z, S_{i+1,j+1}^z \rangle \quad (2)$$

The Hamiltonian cooperates with exchange coupling energy, dipole-dipole interaction, and Zeeman energy along the z-direction.

$$\hat{\mathcal{H}} = -\sum_{i=1}^{N} \left[J_x \hat{\sigma}_i^x \hat{\sigma}_{i+1}^x + J_y \hat{\sigma}_i^y \hat{\sigma}_{i+1}^y + J_z \hat{\sigma}_i^z \hat{\sigma}_{i+1}^z + B_z(\hat{\sigma}_i^z) \right] + \hat{\mathcal{H}}_D \quad (3)$$

$$\hat{\mathcal{H}}_D = \frac{D}{2} \sum_{i=1}^{N} \left[\frac{\hat{\sigma}_i \hat{\sigma}_{i+1}}{r_{i\,i+1}^3} - 3 \frac{(\hat{\sigma}_i . r_{i\,i+1})(\hat{\sigma}_{i+1} . r_{i\,i+1})}{r_{i\,i+1}^5} \right] \quad (4)$$

where $J_\alpha (\alpha: x, y, z)$ is exchange coupling constant, B_z and D represents the magnetic field along the z-axis and the strength of dipole-dipole interaction. The periodic boundary conditions (PBC) are satisfied declaring $\sigma_1 = \sigma_{N+1}$. The abovementioned statistical weight matrix evolves to Equation 5 when the graph configurations are conceptually considered.

$$W_p(S_p) = \sum_{G_p} W_p(S_p, G_p) \quad (5)$$

Gp is a graph variable that has particularly been defined in the plaquette. It has to satisfy $W_p(S_p, G_p) \geq 0$. Graph examples are shown in Figure 1. Gp=1, Gp=2, and Gp=3 graph variables represent the pair flip of any two spins at the edges. $Gp = 4$ indicates that the direction of all spins flips. It is also called a frozen breakup. The rest divides plaquettes into two parts. Frozen breakups induce larger clusters. Note that smaller clusters bring about efficient simulation. Hence, the transition probability to frozen breakups will be low. The graph variables are crucial to deciding whether a transition to a new four-spin state is allowed or not using $\Delta(S_p, G_p)$.

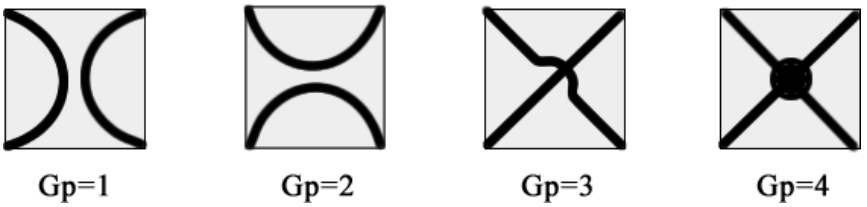

Figure 1. Plaquette breakups of 4-fold spin-1/2 states

The partition function, Z,

$$Z = \sum_S \prod_p W(S_p) = \sum_{S,G} \prod_p W_p(S_p, G_p) \quad (6)$$

$\sum_G$ summation expands the partition function over the entire possible configurations of the graph

Copyright © 2024 IJONFEST

variable. If a plaquette has N number of components, the number of breakups, Nb(N), is defined as in Equation 7 and Equation 8.

$$N_b(N) = \sum_k^N g(N,k) \tag{7}$$

$$\sum_{i=1}^{k} P_i g(N,i) = k^N \quad (k = 1,2,\dots,N) \tag{8}$$

If the spin orientation is changed for a certain breakup, there are multiple spin configurations obtained from a single one. The value of the graph variable Gp defines such a set of spin configurations. The number of GP states increases rapidly to O(αN). This is not very important since the number of states is small enough during the Monte Carlo simulation.

According to Fortuin [65] and Kasteleyn [66], $W(S_p, G_p)$ can be expressed as in Equation 9 where $v_p(G_p)$ is the graph weight of Gp.

$$W_p(S_p, G_p) = v_p(G_p)\Delta(S_p, G_p) \tag{9}$$

$$\Delta(S_p, G_p) = \begin{cases} 1, & S_p \in G_p \\ 0, & others \end{cases} \tag{10}$$

The conventional Monte Carlo Markov chain proposes $S^{(1)} \to S^{(2)} \to S^{(3)} \to \cdots$ in spin configuration space. The spin configuration space follows a graph configuration space in a Markov process of a clustering algorithm. ($S^{(1)} \to G^{(1)} \to S^{(2)} \to G^{(2)} \to S^{(3)} \to G^{(3)} \to \cdots$). The transition probabilities from spin to graphs are explicitly given in Equation 11 and Equation 12.

$$P(S \to G) \equiv \frac{\prod_p W_p(S_p,G_p)}{\sum_{G'} \prod_p W_p(S_p,G_p{}')} \tag{11}$$

$$P(G \to S) \equiv \frac{\prod_p W_p(S_p,G_p)}{\sum_{S'} \prod_p W_p(S'_p,G_p)} \tag{12}$$

$S \equiv \cup_p S_p$ and $G \equiv \cup_p G_p$, represent the global spin and graph configurations, respectively. Each local transition in a plaquette is determined via Equation 13.

$$P(S_p \to G_p) \equiv \frac{W_p(S_p,G_p)}{\sum_{G_p{}'} W_p(S_p,G_p{}')} \tag{13}$$

The transition probabilities noted below are consistent with the detailed balance condition. The probability of any S spin and G graph configuration is defined by Equation 14 and Equation 15.

$$P(S) = \frac{1}{Z}\sum_G \sum_P W_p(S_p, G_p) = \frac{1}{Z}\prod_p W_p(S_p) \tag{14}$$

$$P(G) = \frac{1}{Z}\sum_S \sum_P W_p(S_p, G_p) \tag{15}$$

Since G global graph configurations specify only how the spins are divided in the system, a spin configuration

Copyright © 2024 IJONFEST

can be determined among different configurations according to Equation 12. There are global differences between these spin configurations. In the Monte Carlo process, such a non-local spin orientation change is extracted by every local stochastic decision on every plaquette given by Equation 13. The algorithm that simultaneously updates the spins in clusters is called the cluster algorithm. The clustering algorithm has significant advantages over traditional local spin orientation change algorithms. The binary spin correlation function is identical to the probability function that tells us that these binary lattice points belong to the same cluster. Thus, the clustering algorithm significantly reduces the autocorrelation time between successful Monte Carlo configurations. To ensure ergodicity in quantum models, the Worldlines algorithm requires artificial global spin orientation variation. In the clustering algorithm, only natural global spin orientation variation is present. The loop algorithm can be implemented in both discrete imaginary time and continuous imaginary time. 8 possible quadruple spin configurations are shown in Figure 2.

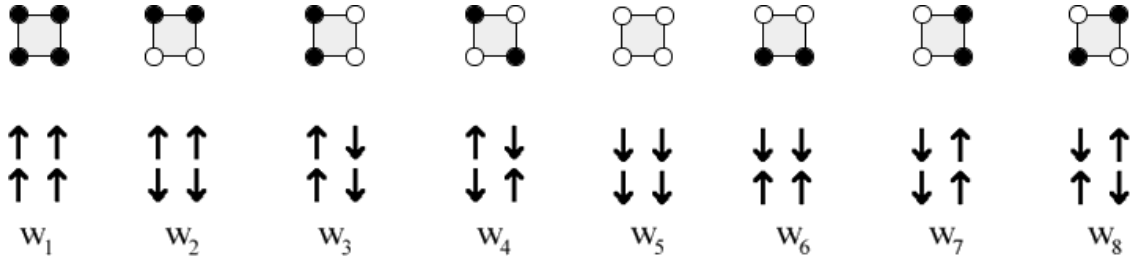

Figure 2. 8 possible 4-fold spin-1/2 states and their vertex weights (Wi): the black dots in the upper row represent upward spins and the white dots represent downward spins.

These configurations and plaquette breakups are illustrated in Figure 3, and Figure 4, respectively. Blackened arrows denote up-spins and gray arrows stand for the down-spins.

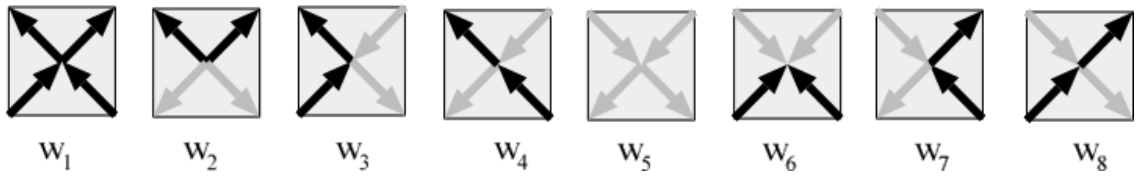

Figure 3. Vertex arrows representation of possible 4-fold spin-1/2 states

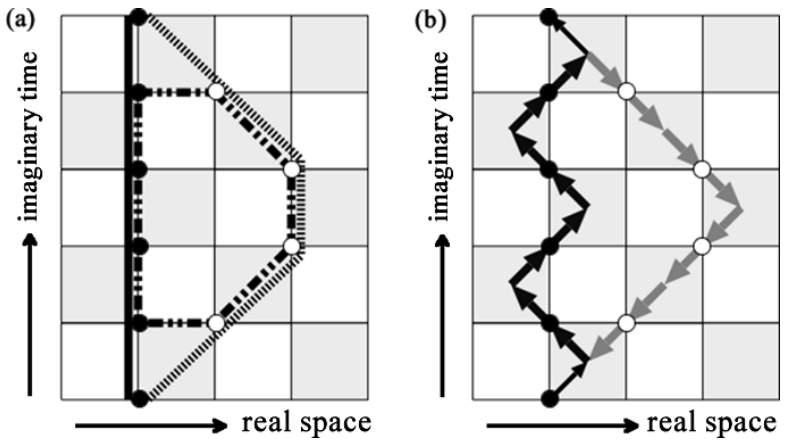

Figure 4. An example of an update of loop algorithm (a) worldline representation (b) vertex arrow representation

Copyright © 2024 IJONFEST

The thick solid line, in Figure 4(a), is a single world line. The dotted line represents a possible cycle. When the spins are reversed throughout the cycle, a dashed worldline is formed. The cycle here is not small enough to be local. Figure 4(b) illustrates the worldline with vertex arrows. The cycle is represented by thick arrows. In vertex representation, each cycle follows the arrows of the spin configuration. In other words, the cycle creates a worldline with upward spins along the imaginary time direction. Downward arrows do not create a world line. The most basic procedure of a Monte Carlo update of the loop algorithm consists of two stochastic mappings: from spins to spins and loops, thence to new spins. A breakup is selected for each shaded (gray) plaquette with the transition probability of the configuration of the spins in the selected plaquette. Clusters are established to create these breaks. When the directions of all arrows are changed along the cycle, each set is reversed with the appropriate probability. Thus, new spin configurations are formed. The value of the probabilities depends on the Hamiltonian and the previous spin configurations. The worldlines are continuous at every site along the Trotter direction due to the imaginary time-space $\Delta\tau \to 0$ ($\frac{\beta}{M} \to 0$) with an occasional jump to neighboring lattice sites. These jumps are instantaneous. $\hat{H}_i$, can be represented by Gp graph variables due to the infinitesimal imaginary time intervals.

$$\langle \varphi_j | \hat{H}_i | \varphi_{j+1} \rangle \equiv -\sum_{G_p} a_p(G_p)\Delta(S_p, G_p) - B_p(S_p) \tag{16}$$

$\Delta(S_p, G_p)$ is as defined in discrete imaginary time. $W_p(S_p)$, vertex weights, takes the form given in Equation 17 for each $\epsilon \equiv \Delta\tau \ll 1$ along continuous imaginary time.

$$W_p(S_p) \equiv \langle \varphi_j | e^{-\Delta\tau \hat{H}_i} | \varphi_{j+1} \rangle \approx e^{-\epsilon B_p(S_p)} \left[I_p(S_p) + \epsilon \sum_{G_p} a_p(G_p)\Delta(S_p, G_p) \right] \tag{17}$$

$I_p(S_p)$, is the unit operator in a plaquette. Taking $\Delta(S_p, 1) \equiv I_p(S_p)$, makes things easier. Taking the limit at $\epsilon \to 0$, a transition probability in a plaquette can be reduced to:

i. If the present S_p the state is consistent with $G_p = 1$ graph, for instance, spin splitting is not available at a $(t, t+\epsilon)$ time interval,

$$P(S_p \to G_p) = \epsilon a_p(G_p)\Delta(S_p, G_p) \qquad (G_p = 1)$$
$$P(S_p \to 1) = 1 - \sum_{G_p' \neq 1} P(S_p \to G_p') \tag{18}$$

ii. If the present S_p the state is inconsistent with $G_p = 1$ graph, for instance, the state at t is different from the state at $t+\epsilon$,

$$P(S_p \to G_p) = \frac{a_p(G_p)\Delta(S_p, G_p)}{\sum_{G_p' \neq 1} a_p(G_p')\Delta(S_p, G_p')} \qquad (G_p = 1)$$
$$P(S_p \to 1) = 0 \tag{19}$$

Eq.18 is applied to plaquette on worldlines along the Trotter direction. The probability of choosing a graph with $G_p \neq 1$ in the imaginary time interval. ϵ is determined by $\epsilon a_p(G_p)\Delta(S_p, G_p)$. In fact, G_p graphs are distributed over a uniform interval with a probability density such as $a_p(G_p)\Delta(S_p, G_p)$ in the continuity limit. On the other hand, Eq.19 specifies the probability expression with the graph relative to the point in time when two neighboring worldlines exchange or a local state change. Note that, the expression here is not probability density.

Copyright © 2024 IJONFEST

The loop algorithm in continuous imaginary time can be generally summarized as follows. For each pair of adjacent world lines,

i. $G_p(\neq 1)$ graphs, as in Equation 18, worldlines are distributed over each imaginary time interval in such a way that they are not overlapped.

ii. At each time point where states can be exchanged between two lattice points, a graph G_p is selected by Equation 19.

iii. $G_p = 1$ is assigned to the rest.

Then the spin values are updated by changing the clusters. This algorithm has some advantages over the loop algorithm in discrete imaginary time. The most important of these is that the need for Trotter extrapolation to reduce the systematic error arising from the finite Trotter number m in Suzuki-Trotter decomposition disappears in the continuity limit. Thus, KMC simulations become more convenient at low temperatures. Discrete imagery can sometimes be implemented more easily on computers than in real-time [57]. The 2-dimensional classical mesh in continuous imaginary time is shown in Figure 5 and Figure 6.

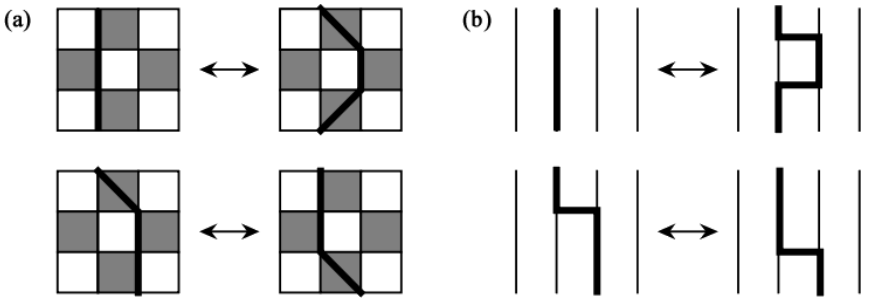

Figure 5. Local update of two worldlines (a) discrete imaginary time (b) continuous imaginary time

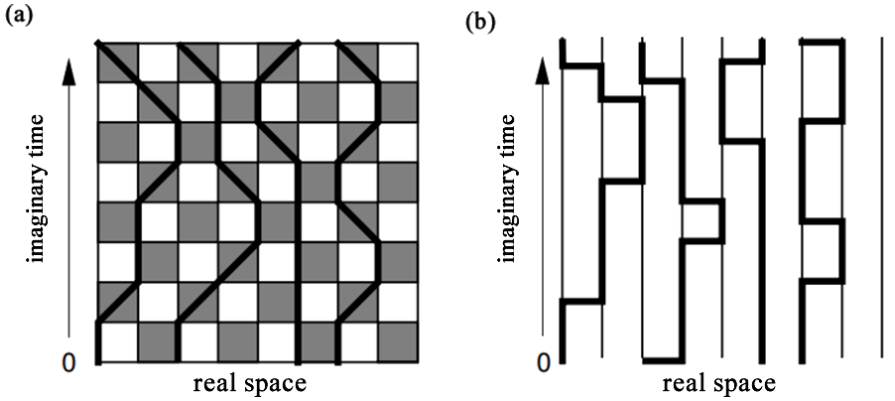

Figure 6. Worldlines (a) discrete imaginary time representation (b) continuous imaginary time representation

A cluster update in continuous imaginary time with the loop algorithm is exemplified in Figure 7.

Copyright © 2024 IJONFEST

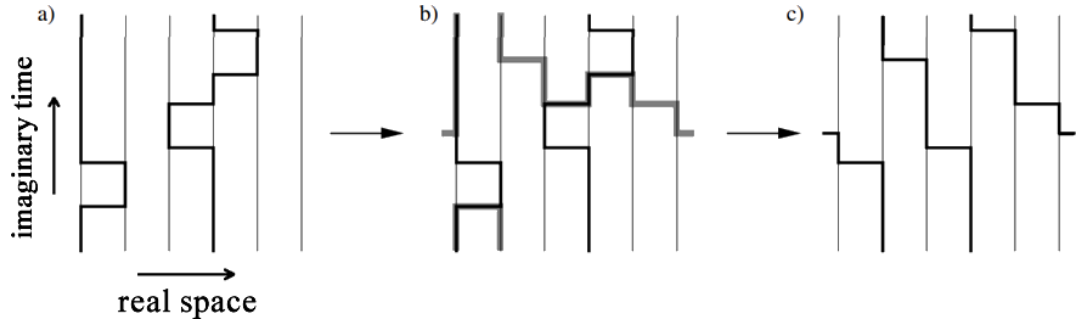

Figure 7. An update scheme of the loop algorithm

Figure 7(a) is the worldlines configuration before an update (thick black lines indicate upward spins, thin gray lines indicate downward spins). In Figure 7(b), there is a cluster update shown with thick gray lines with worldlines configuration. Figure 7(c) shows the world lines configuration after the directions of all spins in the cluster are changed.

2.2 Expected Value & Thermodynamic Quantities

In the lattice model, the partition function and the expected value of an observable are given by Equation 20 and Equation 21 where $\beta = \frac{1}{k_B T}$, T is temperature, and kB is the Boltzmann constant.

$$Z = Tr[e^{-\beta \hat{H}}] \tag{20}$$

$$\langle A \rangle = \frac{Tr[Ae^{-\beta \hat{H}}]}{Tr[e^{-\beta \hat{H}}]} \tag{21}$$

The tough part is to deal with the Hamiltonian of the system in the statistical mechanics of many-particle quantum systems since the observables are in the form of large matrices. It is crucial to represent ⟨A⟩, by vertex weights, W(S), and the A(S) estimators belong to observables to apply the MCMC technique and calculate the expected values,

$$\langle A \rangle = \frac{\sum_S A(S)W(S)}{\sum_S W(S)} \tag{22}$$

In the loop algorithm, the graph configuration G contains a wealth of information about the physical properties of the system. Estimators developed in conjunction with the loop algorithm are used to reduce measurement errors [15, 57]. The expected value of an observable A over G graph, A(G),

$$A(G) = \frac{\sum_S A(S)\Delta(S,G)}{\sum_S \Delta(S,G)} \tag{23}$$

A(G) is the average of A(S) over $2^{N_S(G)}$ number of the worldlines configurations. $N_S(G)$ represents the number of clusters.

Copyright © 2024 IJONFEST

$$\langle A(G)\rangle_G = \frac{1}{Z}\sum_G A(G)W(G) = \frac{1}{Z}\sum_G \left[\frac{\sum_S A(S)\Delta(S,G)}{\sum_S \Delta(S,G)}\right][\sum_S \Delta(S,G)V(G)]$$

$$\langle A(G)\rangle_G = \frac{1}{Z}\sum_S A(S)[\sum_G \Delta(S,G)V(G)] = \langle A(S)\rangle_S \quad (24)$$

The calculation of A(G) calculation is not cost-effective. It can be done more with the help of the symmetries found in an original physical system using improved evaluators. In addition, improved evaluators for correlation functions can be built and the calculation of correlation functions can be facilitated. The significant thermodynamic quantities that are calculated via the improved estimators in this study are given by Equation 25 and Equation 26, respectively. The thermal agitations are included in the atomic scale.

$$M_\alpha = \sum_i S_i^\alpha \qquad (\alpha = x, y, z) \quad \text{(magnetization)} \tag{25}$$

$$E = -\frac{1}{Z}\frac{\partial Z}{\partial \beta} \qquad \text{(internal energy)} \tag{26}$$

2.3 *The Boundaries of the Localizable Entanglement*

The entanglement has been quantified via a variety of measurement approaches, including concurrence, entanglement entropy, entanglement witness, and negativity. Verstraete, F., established a close connection between correlation functions and entanglement by describing localized entanglement between two sub-parts. It is the maximum amount of entanglement that can be localized via making local measurements in the rest of the system using the upper and lower limits. Hence, this content focuses on determining the upper and lower limits of the entanglement of an N-qubit system. Nonetheless, a close relationship between entanglement phenomena and classical correlations has been established. The classical two-point correlation function (Equation 27) is associated with the upper limit [51].

$$Q_{\alpha\beta}^{ij}(|\psi\rangle\langle\psi|) = \langle\psi\left|\hat{\sigma}_\alpha^i \otimes \hat{\sigma}_\beta^j\right|\psi\rangle - \langle\psi|\hat{\sigma}_\alpha^i|\psi\rangle\langle\psi\left|\hat{\sigma}_\beta^j\right|\psi\rangle \tag{27}$$

By unrolling the equation $LE_{ij}(\psi) \geq \max | Q_{\alpha\beta}^{ij}(\psi) |$ for a given pure state $|\psi\rangle$ of N qubits, a relationship between concurrence and localizable entanglement in spin-1/2 systems may be applied to higher-dimensional spin systems. The left side of the Eq.28 is associated with the lower bound of entanglement (LE_{ij}^{lb}) while the right side represents the upper bound of the entanglement (LE_{ij}^{ub}). However, the use of entanglement of assistance (EoA) reveals the upper bound. Thus, the following equation provides an easy way to express the bounds of entanglement.

$$max\left(\left|Q_{xx}^{ij}\right|, \left|Q_{yy}^{ij}\right|, \left|Q_{zz}^{ij}\right|\right) \leq LE_{i,j} \leq \frac{\sqrt{X_+^{ij}}+\sqrt{X_-^{ij}}}{2} \tag{28}$$

$$x_\pm^{ij} = \left(1 \pm \langle\sigma_z^i\sigma_z^j\rangle\right)^2 - \left(\langle\sigma_z^i\rangle \pm \langle\sigma_z^j\rangle\right)^2 \tag{29}$$

A strong methodology based on spin clustering on discrete imaginary time is introduced by loop algorithms as a significant means of simulating quantum spin systems. The Markov process exhibits a continuous loop of the transition from the spin (S) to graph (G) configurations, in contrast to the conventional Markov Chain Monte Carlo (MCMC). The simulation process has been carried out after introducing a spin-1/2 lattice with exchange coupling interactions and the model's Heisenberg Hamiltonian. Long equilibration times can be shortened by gradually lowering the temperature during thermalization. The thermalization cost is 103 of the Monte Carlo steps before the physical quantity measurement method. Here, we concentrated on the internal energy as a function of temperature

Copyright © 2024 IJONFEST

through the MC updates. Simulated data is used to calculate the $Q^{ij}_{\alpha\beta}$ and $x^{ij}_{\pm}$. N=40 quantum spin-1/2 particles are considered as a chain. The thermodynamic properties and the boundaries of entanglement are determined by Loop algorithm-based Quantum Monte Carlo simulation by ALPS package [48] in parallel. The temperature interval has been set to Tϵ(0,4]. The dipole-dipole interaction strength (Dϵ(0,4]) and the external magnetic field ($B_z\epsilon$(0,5]) are taken into account to emphasize the effect of these interactions to the boundaries of entanglement. Note that, exchange coupling constants are set to Jz=1, Jx=Jy=-1.

3. FINDINGS & DISCUSSION

A clear illustration of the spin chain and exchange coupling of a mixed magnetic state is given in Figure 8. FM and AFM states are indicated by Jz, Jx, and Jy couplings in a XXZ mixed state. Jx and Jy specify an AFM interaction while Jz indicates a FM interaction in a spin-1/2 chain. We have previously worked on isotropic AFM [47] and FM models [67] considering the dipole-dipole interaction, and thermal agitations.

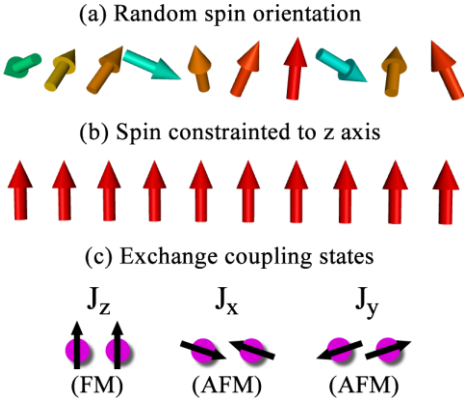

Figure 8. Illustration of spin chain with (a) random spin orientation (b) spin constrained to z-axis (c) exchange coupling constants.

The average magnetization and internal energy per spin as a function of temperature are shown in Figure 9. Firstly, the dipole-dipole interaction is neglected. The spin chain shows ferromagnetic behavior. It is probably originated from ferromagnetic exchange interaction in the -z projection even though antiferromagnetic coupling lies for neighboring spins along the x and y-axis. A stronger external field leads to a higher phase transition temperature (Figure 9(a)). Even the phase seems to be transited, the average magnetization does not vanish. The highest field dominates the thermal agitations, ensuring the spin pairs are constrained along the magnetic field direction. The increasing magnetic field reduces the internal energy (Figure 9(b)). Moreover, increasing temperature causes an increment in internal energy. Under zero fields and lower magnetic fields, the energy gets closer to zero but does not converge, and tends to be zero for infinite temperature.

Copyright © 2024 IJONFEST

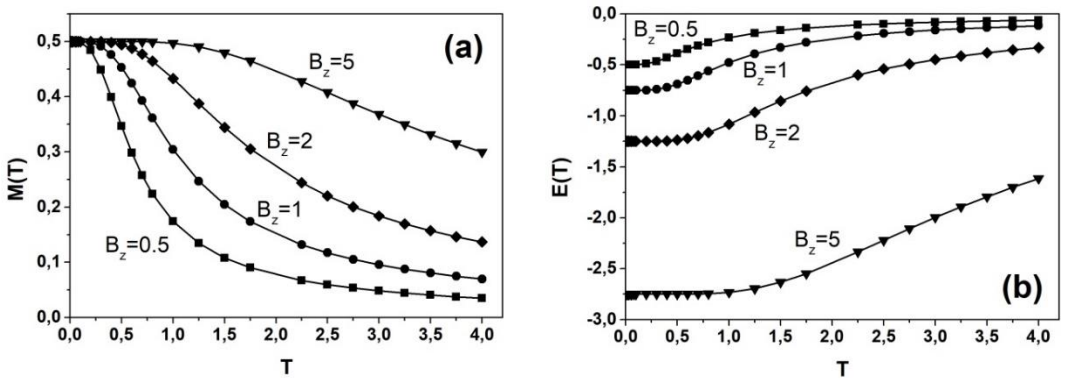

Figure 9. (a) Magnetization per spin (b) internal energy, as a function of temperature under external magnetic field, B_z=0.5, 1, 2, 5.

In the absence of dipole-dipole interaction (D=0), the lower and upper limits of entanglement as a function of temperature under an external magnetic field are clearly shown in Figure 10. The lower limit of entanglement (Figure 10(a)) is inversely proportional to the temperature. The external field contributes to lower limit values of LE. It is more than 3 times the lower limit of B_z=0 at nearly zero temperature. The maximum value of lower limit LE is calculated as 0.25. The strongest field preserves it up to T=1 and inhibits the lower limit from vanishing. There is an analogy between magnetization and lower limit (Figure 10(b)). The upper limit of LE is almost 1 (unity) at every temperature regime in the absence of an external field. Increasing the magnetic field estranges the upper limit from the saturation area. At low temperatures and strong fields, the value of this limit is around 0.75. Consequently, the external field acts directly to the bounds.

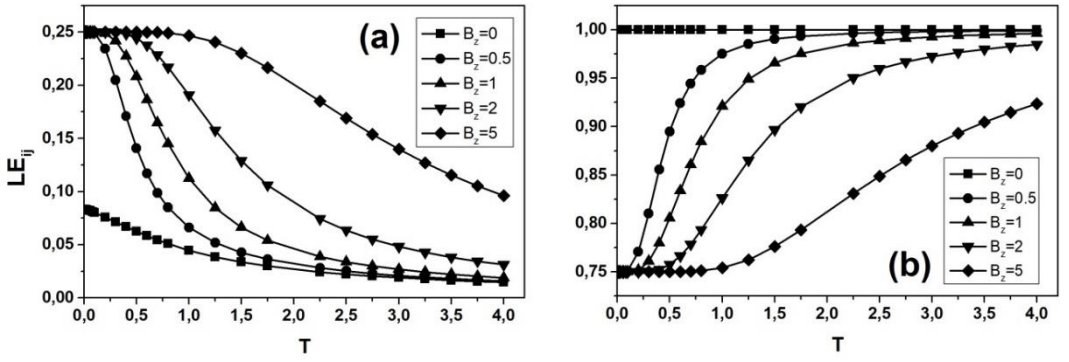

Figure 10. (a) LE lower limit (b) LE upper limit as a function of temperature under external magnetic field, B_z=0.5, 1, 2, 5.

In the absence of external field, lower bound values are decreasing by the increasing dipolar strength for D=0 and D=1 at low temperatures (Figure 11). For D≥1, increasing D hoist the lower limit. The temperature-dependent behavior is monotonic decreasing. We take a sensitive focus on the effect of dipolar strength in the range of D∈(0,1). The lower bound values show a decreasing-increasing behavior, briefly fluctuating, for consecutive temperature values. This can be sort of an awakening phenomenon. Each D creates an individual turning point. The strength of D is a natural tuner of these points as well (Figure 11(b)).

Copyright © 2024 IJONFEST

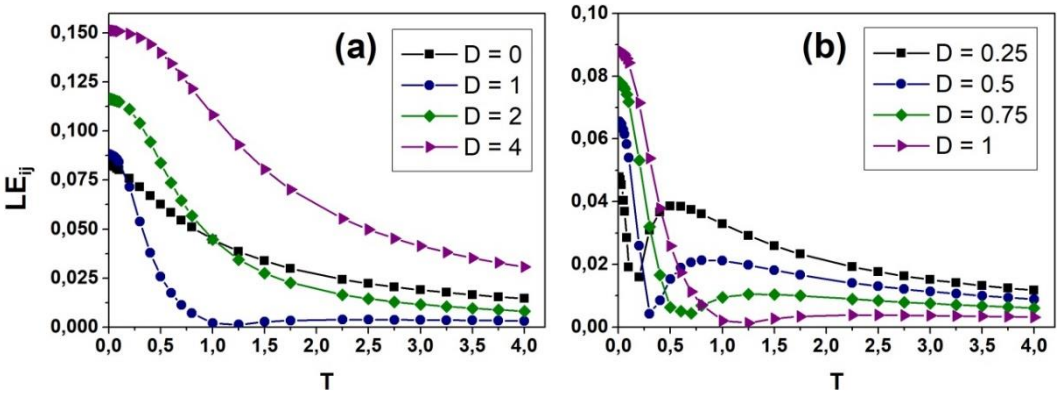

Figure 11. LE lower limit as a function of temperature under zero magnetic field with exchange coupling constants J_x=-1, J_y=-1, J_z=1 for (a) D=0, 1, 2, 4 (b) D= 0.25, 0.5, 0.75, 1.

When B_z=0.5, the lower limit values decrease as D increases in the range 1>D>0. The lowest D value (D=0.25) entails the highest lower limit values at low temperatures. For D>1, it is seen that as D increases, the values of the lower limit increase. D=2 and D=4 are not as entangled at very low temperatures as they are at D=0.25 and D=0.5. However, D=4 resists the distorting effect of temperature and keeps the amount of entanglement farther from zero (see Figure 12).

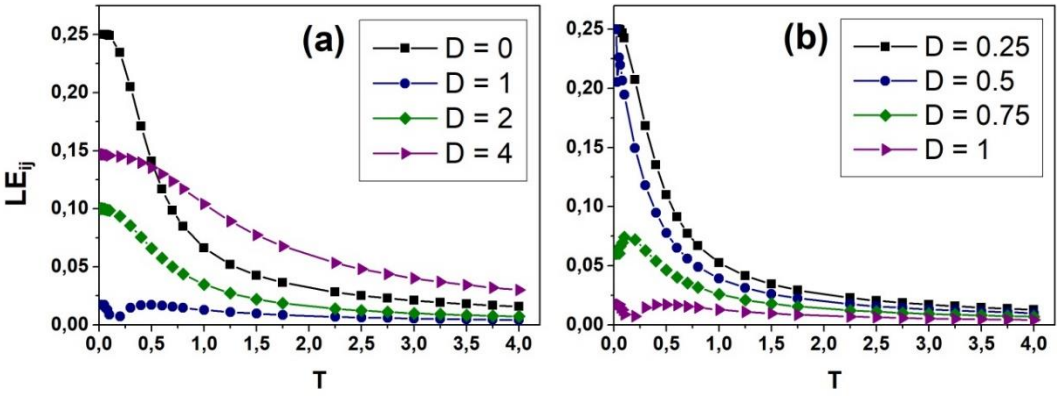

Figure 12. LE lower limit as a function of temperature under B_z=0.5 magnetic field with exchange coupling constants J_x=-1, J_y=-1, J_z=1 for (a) D=0, 1, 2, 4 (b) D= 0.25, 0.5, 0.75, 1.

Copyright © 2024 IJONFEST

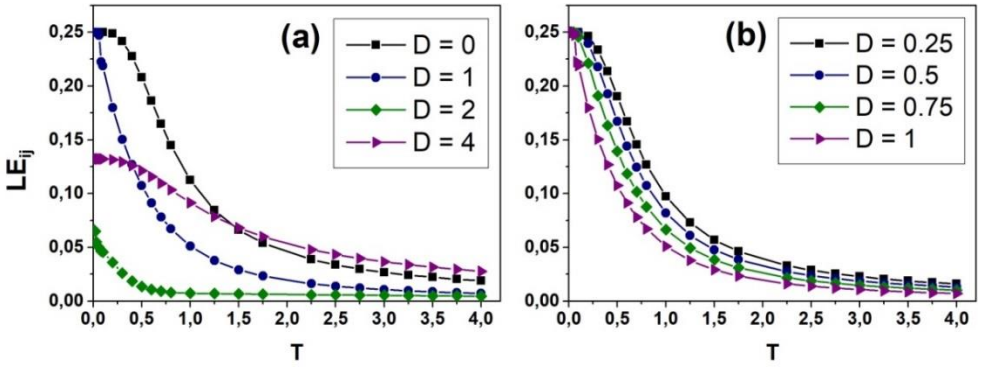

Figure 13. LE lower limit as a function of temperature under B_z=1 magnetic field with exchange coupling constants J_x=-1, J_y=-1, J_z=1 for (a) D=0, 1, 2, 4 (b) D= 0.25, 0.5, 0.75, 1.

The behavior changes as the external field increases. The reason is the dominancy of the external field to the dipolar effect and thermal. The lower limit decreases monotonically (Figure 14 and Figure 15) inverse proportional to the D.

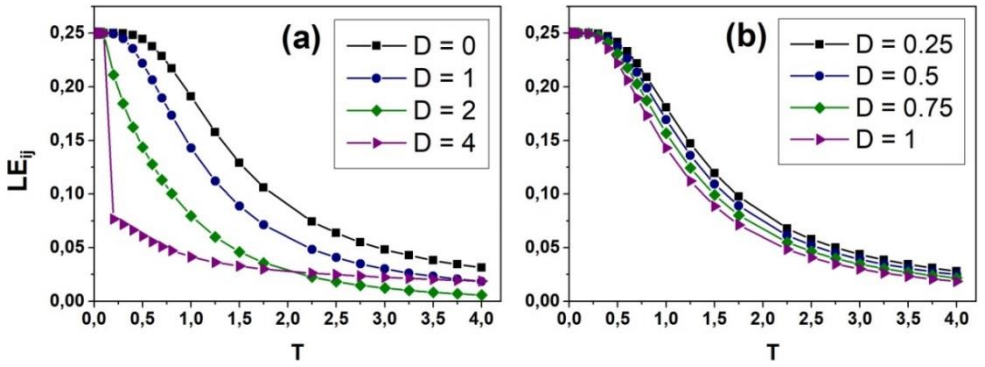

Figure 14. LE lower limit as a function of temperature under B_z=2 magnetic field with exchange coupling constants J_x=-1, J_y=-1, J_z=1 for (a) D=0, 1, 2, 4 (b) D= 0.25, 0.5, 0.75, 1.

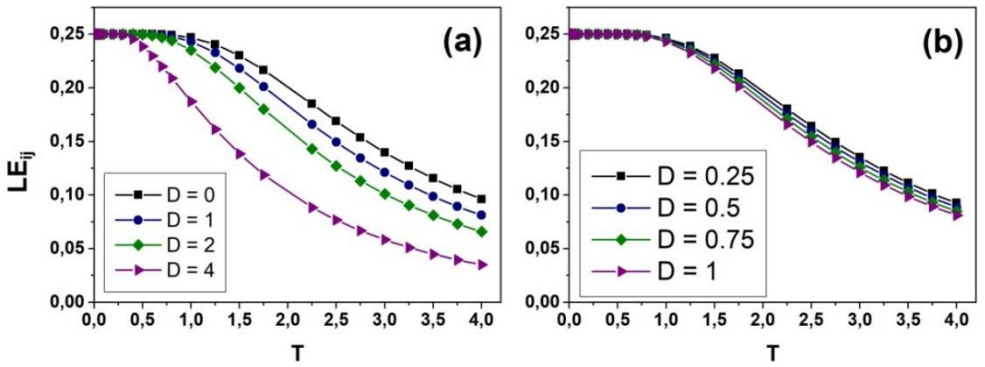

Figure 15. LE lower limit as a function of temperature under B_z=5 magnetic field with exchange coupling constants J_x=-1, J_y=-1, J_z=1 for (a) D=0, 1, 2, 4 (b) D= 0.25, 0.5, 0.75, 1.

Copyright © 2024 IJONFEST

The upper limit has its maximum value for all D values in the absence of an external field (Figure 17). As the external field increases, the upper limit decreases for lower temperatures as D decreases for T≥1.5; besides, they all overlap at the maximum value. Although this behavior does not change for 5>Bz≥0, the value of the T temperature at which all D curves begin to overlap increases. When B_z=5, the upper limit values corresponding to all D values decrease and reach their maximum with temperature and do not overlap.

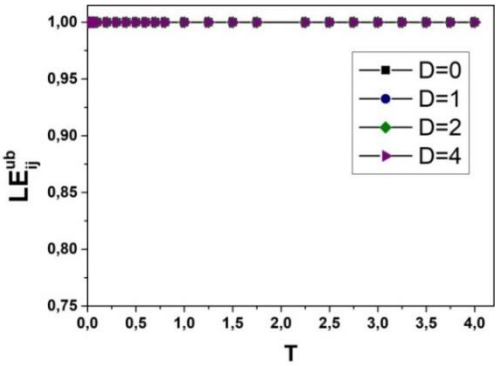

Figure 17. The upper limit of localizable entanglement under zero magnetic field for exchange coupling constants J_x=-1, J_y=-1, J_z=1 and dipolar interaction with D=0, 1, 2, 4.

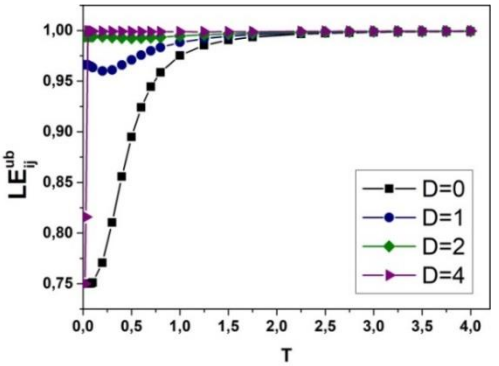

Figure 18. The upper limit of localizable entanglement under B_z=0.5 magnetic field for exchange coupling constants J_x=-1, J_y=-1, J_z=1 and dipolar interaction with D=0, 1, 2, 4.

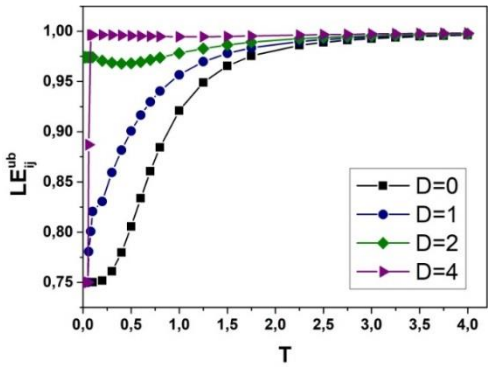

Figure 19. The upper limit of localizable entanglement under B_z=1 magnetic field for exchange coupling constants J_x=-1, J_y=-1, J_z=1 and dipolar interaction with D=0, 1, 2, 4.

Copyright © 2024 IJONFEST

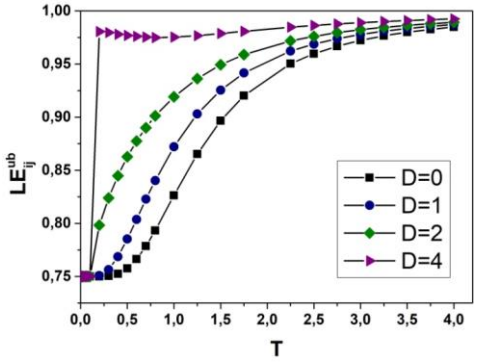

Figure 20. The upper limit of localizable entanglement under B_z=2 magnetic field for exchange coupling constants J_x=-1, J_y=-1, J_z=1 and dipolar interaction with D=0, 1, 2, 4.

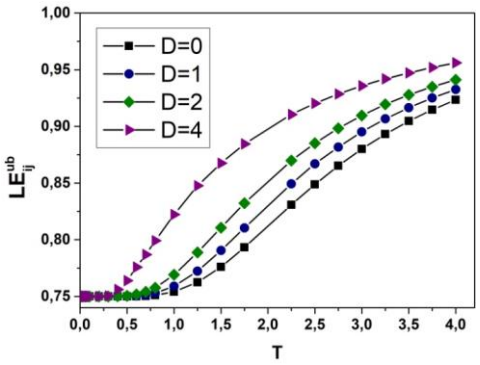

Figure 21. The upper limit of localizable entanglement under B_z=5 magnetic field for exchange coupling constants J_x=-1, J_y=-1, J_z=1 and dipolar interaction with D=0, 1, 2, 4.

Localizable entanglement between nearest neighboring spins is determined through lower and upper bounds for mixed magnetic states. The distance-dependent entanglement is discussed including the temperature and external field. In the absence of field (B_z = 0), LE of neighboring 20 spins is gradually measured (Figure 22). D = 4 dominates the thermal effects maximizing the lower bounds except T = 3.5. At very high temperatures (T = 3.5), this behavior does not change but is not at its maximum value. Accordingly, it can be said that as the temperature increases, the lower limit does not change according to the distance for D=4. The situation is slightly different for other dipole constants. In the absence of dipole-dipole interaction at T = 0.1, the lower limit of the entanglement is not damped until n = 10 adjacent spins. At T = 0.5 temperature, the distortion effect of temperature reduced the number of spins of the nearest n = 10 neighbors entangled for D = 0. At T ≥ 1 temperature, the lower limit is damped for all D values starting from the 2nd adjacent spin. When D < 4, the distorting effect of temperature dominates the dipole-dipole interaction.

Copyright © 2024 IJONFEST

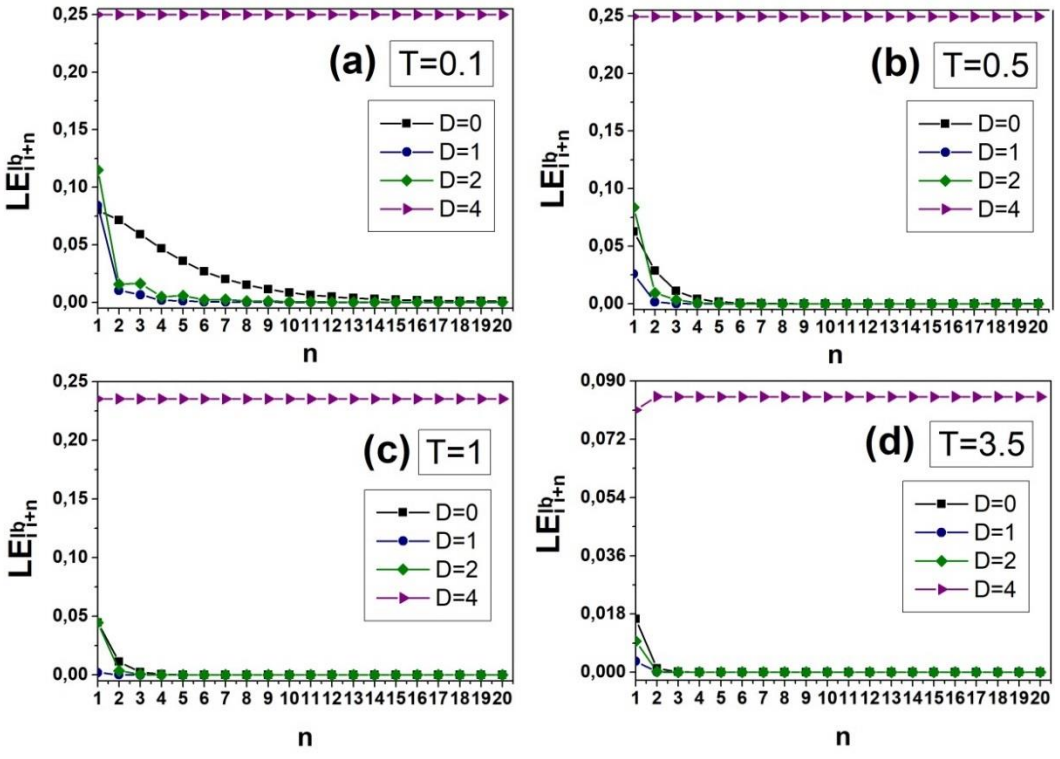

Figure 22. The lower limit of LE under zero magnetic field for 20 nearest neighboring at temperatures (a) T=0.1 (b) T=0.5 (c) T=1 (d) T=3.5

According to Figure 22(c) ($D = 2$), there is non-monotonic LE_{ij}^{lb} values underlying "rival regions" at low temperatures and under low magnetic fields.

Copyright © 2024 IJONFEST

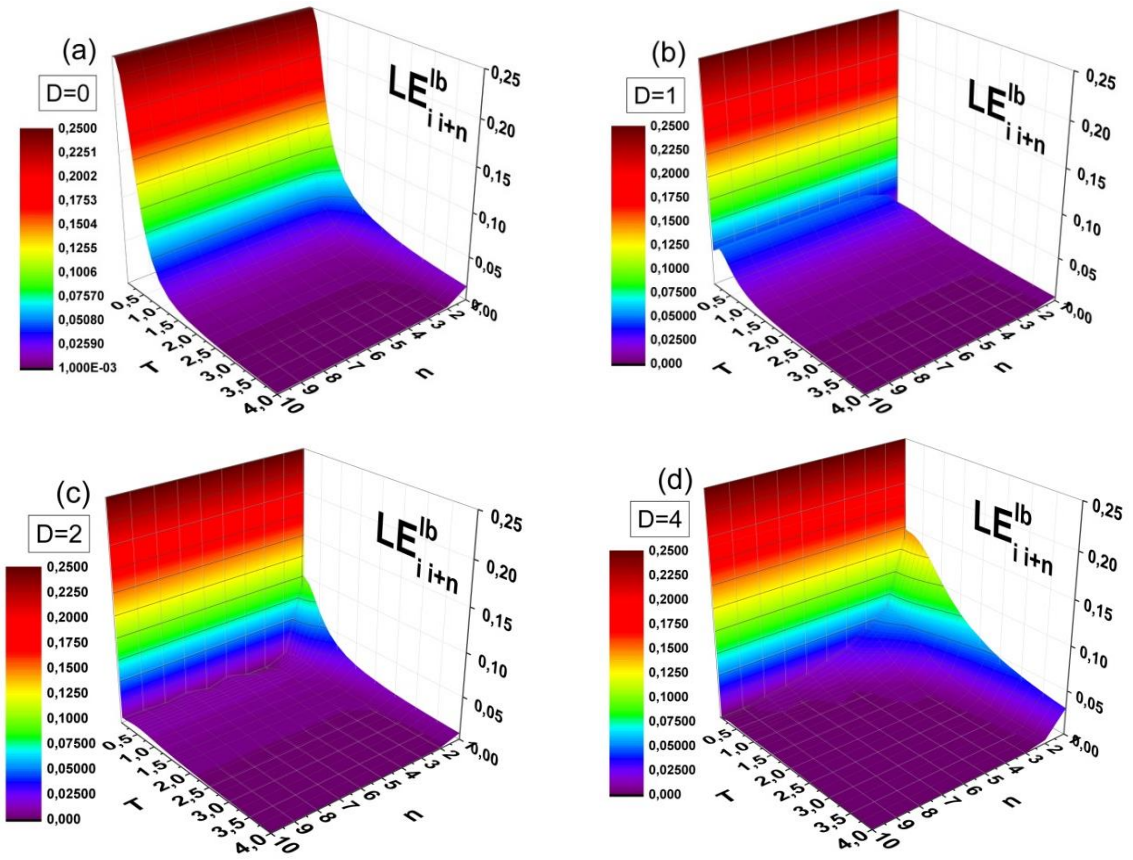

Figure 23. The illustration of the lower limit of LE under B_z=0.5 magnetic field for 10 nearest neighboring spins.

The variation of the lower limit of entanglement with temperature according to the nth neighboring spins under the external magnetic field B_z = 0.5 is given in Figure 23 for D = 0, 1, 2, and 4, respectively. At B_z = 0.5, for D = 0, the behavior of the first 10 neighboring spins with temperature is monotonous but does not change according to the length at low temperatures. At D = 1, the lower limit for all neighboring spins suddenly fell at low temperatures and, immediately after, increased until T = 0.5. At these low temperatures, the first and second neighboring spins, n=1 and n=2, have subdued lower bound values than the rest. D = 4 is the strength where the lower limit is maximized at both high and low temperatures. Except for D = 4 and B_z = 2, all other D strengths do not affect the system. D=4 causes a weak odd-even effect for n = 4. However, as D increases, the lower limit values decrease related to temperature and n. The change of the lower limit of entanglement with temperature according to the number of nth neighbors under the external magnetic field B_z = 2 is given in Figure 24 for D = 0, 1, 2, and 4, respectively. In the absence of a dipolar interaction, an external field merely takes place and influences the bounds of entanglement. As shown in Figure 24(a), there is a monotonic behavior in which LE decreases by increasing temperature for all nth neighboring spins except the nearest one. This discrepancy is abolished through the existence of dipolar interaction. According to Figure 24(d) ($D = 4$), there is non-monotonic LE_{ij}^{lb} values pointing to "revival regions" at low temperatures under low magnetic fields. Note that n=3 (3rd neighboring spins) is a clear fluctuation point that the value of the lower limit abruptly changes.

Copyright © 2024 IJONFEST

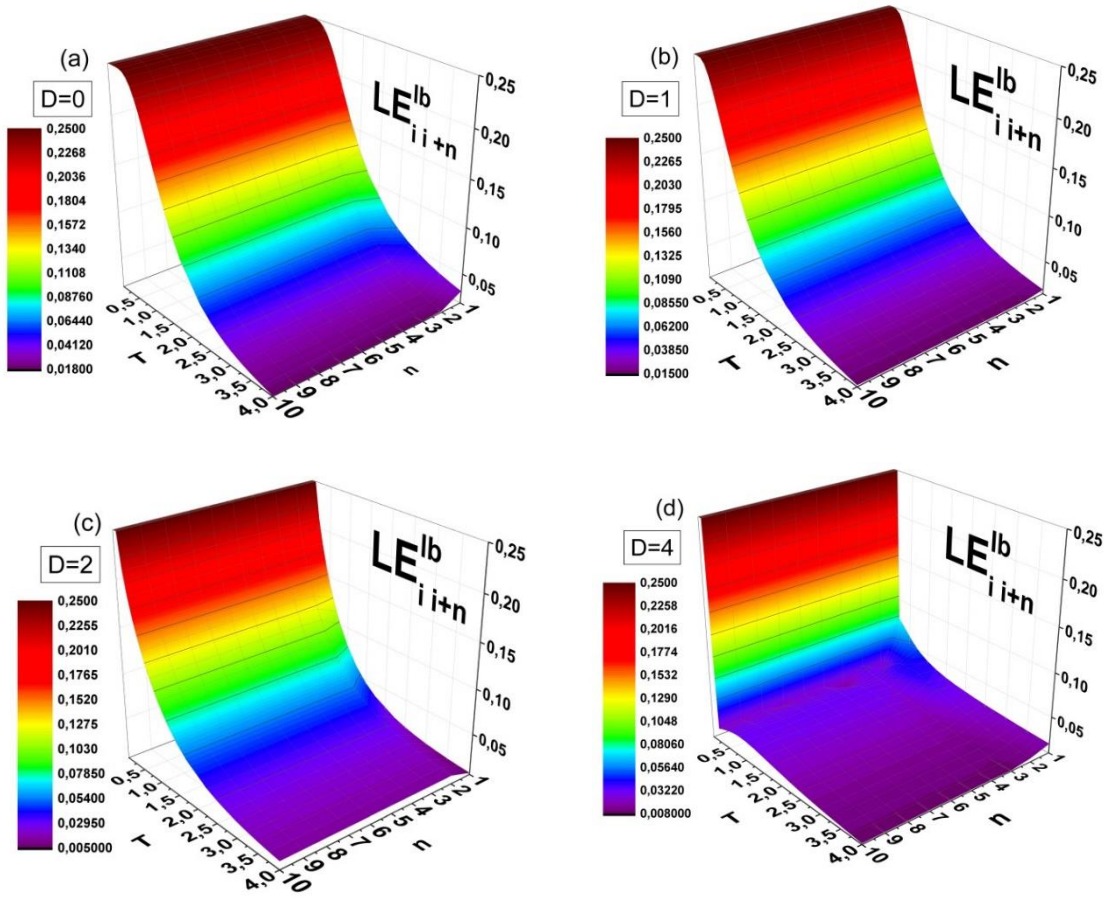

Figure 24. The illustration of the lower limit of LE under B_z=2 magnetic field for 10 nearest neighboring spins.

4. CONCLUSION

The upper and lower bounds of LE are quantified to measure entanglement between any two parts of the multipartite XXZ spin chain. In the T→0 case, the lower bound possesses a monotonically increasing trend proportional to the applied field when dipole-dipole interaction is disregarded. This behavior works for increasing temperature. As expected, thermal agitations distort the lower bound, and non-monotonic behavior takes place at relatively low temperatures. In the absence of dipole-dipole interaction at T = 0.1, the lower limit of the entanglement is not damped until n = 10 adjacent spins. At T = 0.5, the distortion effect of temperature reduced the number of spins of the nearest n = 10 neighbors entangled for D = 0. There is a monotonic behavior in which LE decreases by increasing temperature for all nth neighboring spins except the nearest one under when D = 0 under B_z = 0.5 magnetic field while a non-monotonic attitude points to rival regions at low temperatures.

Acknowledgments

This research was supported by the Scientific Research Projects Commission of Marmara University (FEN-C-DRP-120613-0273). Simulations were performed in the Simulation and Modeling Research Laboratory (Simulab) at the Department of Physics, Marmara University.

Copyright © 2024 IJONFEST

Funding

The authors should declare the financial interests which may be considered as potential competing interests.

Declaration of Competing Interest

Competing interest statement declared by authors. This statement must also appear in your manuscript before the references.

References

[1] Modławska, J., & Grudka, A., (2008). Nonmaximally Entangled States Can Be Better for Multiple Linear Optical Teleportation. *Physical Review Letters, 100, 110503.*

[2] Cavalcanti, D., Skrzypczyk, P., & Šupić, I., (2017).All Entangled States can Demonstrate Nonclassical Teleportation. *Physical Review Letters, 119, 110501.*

[3] Z.A.Sabegh, R., & Mahmoudi, M., (2018). Spatially dependent atom-photon entanglement. *Scientific Reports, 8, 13840.*

[4] Loss, D., & DiVincenzo, D., (1998). Quantum computation with quantum dots. *Physical Review A, 57, 120.*

[5] Jürgen Audretsch (2007), The Quantum Computer. In Entangled Systems: New Directions in Quantum Physics *(pp.219-245), Weinheim, Germany: John Wiley and Sons, Ltd.*

[6] Belsley, M. (2014). Introduction to Quantum Information Science, by Vlatko Vedral. *Contemporary Physics, 55, 124.*

[7] DiVincenzo, D. (1997). Quantum computation and spin physics (invited). *Journal of Applied Physics, 81, 4602-4607.*

[8] Zheng, S., & Guo, G., (2000). Efficient Scheme for Two-Atom Entanglement and Quantum Information Processing in Cavity QED. *Physical Review Letters, 85, 2392-2395.*

[9] Bennett, C., & DiVincenzo, D., (2000). Quantum information and computation. *Nature, 404, 1476-4687.*

[10] Eggert, S., Affleck, I., & Takahashi, M., (1994). Susceptibility of the spin 1/2 Heisenberg antiferromagnetic chain. *Physical Review Letters, 73, 332-335.*

[11] Hammar, P., Stone, M., Reich, D., Broholm, C., Gibson, P., Turnbull, M., Landee, C., & Oshikawa, M., (1999). Characterization of a quasi-one-dimensional spin-1/2 magnet which is gapless and paramagnetic for $g\,\mu\,B\,H \lesssim J$ and $k_B T \ll J$. *Physical Review B, 59, 1008-1015.*

[12] Androvitsaneas, P., Fytas, N., Paspalakis, E., & Terzis, A.F., (2012). Quantum Monte Carlo simulations revisited: The case of anisotropic Heisenberg chains. *Philosophical Magazine, 92, 4649-4656.*

[13] Barma, M., & Shastry, B., (1978). Classical equivalents of one-dimensional quantum-mechanical systems. *Physical Review B, 18, 3351-3359.*

[14] Handscomb, D. (1964). A Monte Carlo method applied to the Heisenberg ferromagnet. *Mathematical Proceedings of the Cambridge Philosophical Society, 60, 115-122.*

[15] Harada, K., & Kawashima, N., (2001). Loop Algorithm for Heisenberg Models with Biquadratic Interaction and Phase Transitions in Two Dimensions. *Journal of the Physical Society of Japan, 70, 13-16.*

[16] Huang, Y., & Su, G., (2017). Quantum Monte Carlo study of the spin-1/2 honeycomb Heisenberg model with mixed antiferromagnetic and ferromagnetic interactions in external magnetic fields. *Physical Review E, 95, 052147.*

[17] Sandvik, A., & Kurkijärvi, J., (1991). Quantum Monte Carlo simulation method for spin systems. *Physical Review B, 43, 5950-5961.*

[18] Deger, C., Aksu, P., & Yildiz, F., (2016). Effect of Interdot Distance on Magnetic Behavior of 2-D Ni Dot Arrays. *IEEE Transactions on Magnetics, 52, 1-4.*

[19] Duru, I., Değer, C., Kalaycı, T., & Arucu, M., (2015). A computational study on magnetic effects of $Zn_{1-x}Cr_xO$ type diluted magnetic semiconductor. *Journal of Magnetism and Magnetic Materials, 396 pp. 268-274.*

[20] Arnesen, M., Bose, S., & Vedral, V., (2001). Natural Thermal and Magnetic Entanglement in the 1D Heisenberg Model. *Physical Review Letters, 87, 017901.*

[21] Marchukov, O.V., & Zinner, N., (2016). Quantum spin transistor with a Heisenberg spin chain. *Nature Communications, 7, 13070.*

[22] Renes, J., Miyake, A., Brennen, G., & Bartlett, S., (2013). Holonomic quantum computing in symmetry-protected ground states of spin chains. *New Journal of Physics, 15, 025020.*

[23] Apollaro, T., Lorenzo, S., Sindona, A., Paganelli, S., Giorgi, G., & Plastina, F., (2015). Many-qubit quantum state transfer via spin chains. *Physica Scripta, T165 pp. 014036.*

[24] Wang, X., (2002). Threshold temperature for pairwise and many-particle thermal entanglement in the isotropic Heisenberg model. *Physical Review A, 66, 044305.*

[25] Wang, X., (2001). Entanglement in the quantum Heisenberg XY model. *Physical Review A, 64, 012313.*

[26] Rigolin, G., (2004). Thermal entanglement in the two-qubit Heisenberg XYZ model. *International Journal of Quantum Information, 2, 393-405.*

Copyright © 2024 IJONFEST

[27] Androvitsaneas, P., Paspalakis, E., & Terzis, A., (2012). A quantum Monte Carlo study of the localizable entanglement in anisotropic ferromagnetic Heisenberg chains. *Annals of Physics, 327, 212-223.*

[28] Sinyagin, A., Belov, A., Tang, Z., & Kotov, N., (2006). Monte Carlo Computer Simulation of Chain Formation from Nanoparticles. *Journal of Physical Chemistry B, 110, 7500-7507.*

[29] Kim, I., (2013). Long-Range Entanglement is Necessary for a Topological Storage of Quantum Information. *Physical Review Letters, 111, 080503.*

[30] Elman, S., Bartlett, S., & Doherty, A., (2017). Long-range entanglement for spin qubits via quantum Hall edge modes. *Physical Review B, 96, 115407.*

[31] Bitko, D., Rosenbaum, T., & Aeppli, G., (1996). Quantum Critical Behavior for a Model Magnet. *Physical Review Letters, 77, 940-943.*

[32] Chakraborty, P., Henelius, P., Kjønsberg, H., Sandvik, A., & Girvin, S., (2004). Theory of the magnetic phase diagram of $LiHoF_4$. *Physical Review B, 70, 144411.*

[33] Bramwell, S., & Gingras, M., (2001). Spin Ice State in Frustrated Magnetic Pyrochlore Materials. *Science, 294, 1495-1501.*

[34] Castelnovo, C. R., & Sondhi, S., (2008). Magnetic Monopoles in Spin Ice. *Nature, 451, 42-45.*

[35] Mengotti, E., Heyderman, L., Bisig, A., Fraile Rodríguez, A., Le Guyader, L., Nolting, F., & Braun, H., (2009). Dipolar energy states in clusters of perpendicular magnetic nanoislands. *Journal of Applied Physics, 105, 113113.*

[36] Lahaye, T., Menotti, C., Santos, L., Lewenstein, M., & Pfau, T., (2009). The physics of dipolar bosonic quantum gases. *Reports on Progress in Physics. 72, 126401.*

[37] Peter, D., Müller, S., Wessel, S., & Büchler, H., (2012). Anomalous Behavior of Spin Systems with Dipolar Interactions. *Physical Review Letters, 109, 025303.*

[38] Islam, R., Senko, C., Campbell, W., Korenblit, S., Smith, J., Lee, A., Edwards, E., Wang, C., Freericks, J., & Monroe, C., (2013). Emergence and Frustration of Magnetism with Variable-Range Interactions in a Quantum Simulator. *Science, 340, 583-587.*

[39] Jurcevic, P., & Roos, C., (2014). Quasiparticle engineering and entanglement propagation in a quantum many-body system. *Nature, 511, 202-205.*

[40] Richerme, P., & Monroe, C., (2014). Non-local propagation of correlations in quantum systems with long-range interactions. *Nature, j511 pp. 198-201.*

[41] Mahmoudian S., Rademaker L., Ralko A., Fratini S., & Dobrosavljevic V., (2015). Glassy Dynamics in Geometrically Frustrated Coulomb Liquids without Disorder. *Physical Review Letters, 115, 025701.*

[42] Bohnet, J., Sawyer, B., Britton, J., Wall, M., Rey, A., Foss-Feig, M., & Bollinger, J., (2016). Quantum spin dynamics and entanglement generation with hundreds of trapped ions. *Science, 352, 1297-1301.*

[43] Sahling, S., & Lorenzo, E., (2015). Experimental realization of long-distance entanglement between spins in antiferromagnetic quantum spin chains. *Nature Physics, 15, 255-260.*

[44] Osborne, T., & Nielsen, M., (2002). Entanglement in a simple quantum phase transition. *Physical Review A, 66, 032110.*

[45] Vidal, G., Latorre, J., Rico, E., & Kitaev, A., (2003). Entanglement in Quantum Critical Phenomena. *Physical Review Letters, 90, 227902.*

[46] Bravo, B., Cabra, D., Gomez Albarracin, F., & Rossini, G., (2017). Long−range interactions in antiferromagnetic quantum spin chains. *Physical Review B, 96, 054441.*

[47] Duru, I.P., & Aktas, S., (2019). Localizable entanglement of isotropic antiferromagnetic spin-1/2 chain. *Turkish Journal of Physics. 43 pp. 272 - 279.*

[48] Bauer, B., Carr, L., Evertz, H., Feiguin, A., Freire, J., Fuchs, S., Gamper, L., Gukelberger, J., Gull, E., Guertler, S., Hehn, A., Igarashi, R., Isakov, S., Koop, D., Ma, P., Mates, P., Matsuo, H., Parcollet, O., Pawlowski, G., Picon, J., Pollet, L., Santos, E., Scarola, V., Schollwöck, U., Silva, C., Surer, B., Todo, S., Trebst, S., Troyer, M., Wall, M., Werner, P., & Wessel, S., (2011). The ALPS project release 2.0: open source software for strongly correlated systems. *Journal of Statistical Mechanics: Theory and Experiment, 2011, P05001.*

[49] DiVincenzo & Uhlmann, A., (1999). Entanglement of Assistance. *Quantum Computing and Quantum Communications, pp. 247-257.*

[50] Laustsen, T., Verstraete, F., & Van Enk, S., (2003). Local vs. Joint Measurements for the Entanglement of Assistance. *Quantum Information and Computation, 3, 64-83.*

[51] Popp, M., Verstraete, F., Martin-Delgado, M., & Cirac, J., (2005). Localizable entanglement. *Physical Review A, 71, 042306.*

[52] Todo, S., & Kato, K., (2001). Cluster Algorithms for General S Quantum Spin Systems. *Physical Review Letters, 87, 047203.*

[53] Vedral, V., & Plenio, M., (1998). Entanglement measures and purification procedures. *Physical Review A, 57, 1619-1633.*

[54] Qi, X., Gao, T., & Yan, F., (2017). Lower bounds of concurrence for N-qubit systems and the detection of k-nonseparability of multipartite quantum systems. *Quantum Information Process, 16, 23.*

[55] Xue-Na Zhu, M., & Fei, S., (2018). A lower bound of concurrence for multipartite quantum systems. *Quantum Information Processing, 17, 30.*

[56] Cornelio, M., (2013). Multipartite monogamy of the concurrence. *Physical Review A, 87, 032330.*

[57] Evertz, H. G., Lana, G., & Marcu, M. (1993). Cluster algorithm for vertex models. Physical Review Letters, 70(7), 875.

[58] Evertz, H. G., & Marcu, M. (1993). The loop-cluster algorithm for the case of the 6 vertex model. Nuclear Physics B-Proceedings Supplements, 30, 277–280.

[59] Kawashima, N., Gubernatis, J. E., & Evertz, H. G. (1994). Loop algorithms for quantum simulations of fermion models on lattices. Physical Review B, 50(1), 136.

[60] Sandvik, A. W. (1992). A generalization of Handscomb's quantum Monte Carlo scheme-application to the 1D Hubbard model. Journal of Physics A: Mathematical and General, 25(13), 3667.

Copyright © 2024 IJONFEST

[61] Sandvik, A. W. (1997). Finite-size scaling of the ground-state parameters of the two-dimensional Heisenberg model. Physical Review B, 56(18), 11678.
[62] Sandvik, A. W., & Kurkijärvi, J. (1991). Quantum Monte Carlo simulation method for spin systems. Physical Review B, 43(7), 5950.
[63] Scalettar, R. T. (1998). World-line quantum Monte Carlo. Quantum Monte Carlo Methods in Physics and Chemistry, 525, 65.
[64] Swendsen, R. H., & Wang, J.-S. (1987). Nonuniversal critical dynamics in Monte Carlo simulations. Physical Review Letters, 58(2), 86.
[65] Fortuin, C. M. (1969). Physica (Utrecht) 57, 536 (1972); PW Kasteleyn and CM Fortuin. J. Phys. Soc. Jpn. Suppl, 26(11).
[66] Fortuin, C. M., & Kasteleyn, P. W. (1972). On the random-cluster model: I. Introduction and relation to other models. Physica, 57(4), 536–564.
[67] Duru, İ.P., & Aktaş, Ş. (2022). Dipole-Dipole Effect to Limits of Entanglement in Multipartite Spin Chain: A Monte Carlo Study. International Journal of Advances in Engineering and Pure Sciences, 34(2), 305-316. https://doi.org/10.7240/jeps.1032914

Copyright © 2024 IJONFEST